

Spatial distribution of C₄H and *c*-C₃H₂ in cold molecular cores

YIJIA LIU,¹ JUNZHI WANG,² SHU LIU,³ NINGYU TANG,¹ YAN GONG,⁴ YUQIANG LI,⁵ JUAN LI,⁵ RUI LUO,² AND YANI XU²

¹*Department of Physics, Anhui Normal University, Wuhu, Anhui 241002, People's Republic of China*

²*Guangxi Key Laboratory for Relativistic Astrophysics, Department of Physics, Guangxi University, Nanning 530004, PR China*

³*National Astronomical Observatories, Chinese Academy of Sciences, Beijing 100101, People's Republic of China*

⁴*Max-Planck-Institut für Radioastronomie, Auf dem Hügel 69, 53121, Bonn, Germany*

⁵*Shanghai Astronomical Observatory, 80 Nandan Road, Shanghai 200030, China*

ABSTRACT

C₄H and *c*-C₃H₂, as unsaturated hydrocarbon molecules, are important for forming large organic molecules in the interstellar medium. We present mapping observations of C₄H ($N=9-8$) lines, *c*-C₃H₂ ($J_{Ka,Kb}=2_{1,2}-1_{0,1}$) and H¹³CO⁺ ($J=1-0$) toward 19 nearby cold molecular cores in the Milky Way with the IRAM 30m telescope. C₄H 9-8 was detected in 13 sources, while *c*-C₃H₂ was detected in 18 sources. The widely existing C₄H and *c*-C₃H₂ molecules in cold cores provide material to form large organic molecules. Different spatial distributions between C₄H 9-8 and *c*-C₃H₂ 2-1 were found. The relative abundances of these three molecules were obtained under the assumption of local thermodynamic equilibrium conditions with a fixed excitation temperature. The abundance ratio of C₄H to *c*-C₃H₂ ranged from 0.34 ± 0.09 in G032.93+02 to 4.65 ± 0.50 in G008.67+22. A weak correlation between C₄H/H¹³CO⁺ and *c*-C₃H₂/H¹³CO⁺ abundance ratios was found, with a correlation coefficient of 0.46, which indicates that there is no tight astrochemical connection between C₄H and *c*-C₃H₂ molecules.

Keywords: Astrochemistry (75) — Interstellar molecules (849) — Chemical abundances (224) — Abundance ratios(11)

1. INTRODUCTION

Organic molecules are important complex molecules in the interstellar medium (ISM). Hydrocarbons, the simplest organic molecules, have been recognized as ubiquitous in the ISM since the 1970s (Tucker et al. 1974; Thaddeus et al. 1985; Yamamoto et al. 1987). Small unsaturated hydrocarbon molecules, such as C₂H, C₂H₂, C₄H, C₆H, *l*-C₃H₂ and *c*-C₃H₂, are very important for the formation of large organic molecules. Due to their permanent dipole moments and relatively high abundances, C₄H and *c*-C₃H₂, which can form in cold molecular cores, have been detected in cold dark clouds such as TMC-1 (Irvine et al. 1981; Matthews & Irvine 1985; Madden et al. 1989).

C₄H is the simplest example of a polyne, an organic substance with alternating single- and triple-bond positions in the molecular structure (Cuadrado et al. 2015). It was first detected in the circumstellar envelopes of carbon-rich evolved stars (Guélin et al. 1978) and then in very different environments, eg., cold dark clouds (Irvine et al. 1981; Gottlieb et al. 1985) and diffuse medium (Bell et al. 1983). Based on several chemical networks, C₄H can be formed by some routes for the C_{*n*}H family and through the reaction of C with *l*-C₃H₂ (Loison et al. 2014; Remijan et al. 2023). Meanwhile, C₄H can undergo destruction to form C₄H⁻ through the radiation absorption of an electron (Harada & Herbst 2008; Gianturco et al. 2016). *c*-C₃H₂ is a cyclic structure with an isomer, the linear *l*-C₃H₂. The cyclic isomer *c*-C₃H₂ exhibits greater stability and higher abundance compared to the linear counterpart *l*-C₃H₂. As the first organic ring in the ISM, *c*-C₃H₂ was first detected in Sgr B2 (OH) (Thaddeus et al. 1985) and subsequently found in other sources (Fossé et al. 2001; Sakai et al. 2010; Pety et al. 2012). *c*-C₃H₂ can be formed through dissociative recombination of C₃H₃⁺ (Herbst et al. 1984; Smith & Adams 1987; Park et al. 2006) and the reaction between *l*-C₃H₂ and H (Loison et al. 2017). In dense molecular clouds, the reaction of *c*-C₃H₂ with O forms HC₃O (Loison et al. 2017).

Although hydrogen is much more abundant than carbon in interstellar clouds, the abundance of C_4H ($\sim 2.8 \times 10^{-9}$) and $c\text{-}C_3H_2$ ($\sim 2.8 \times 10^{-10}$) compared to molecular hydrogen is relatively high (Zhang et al. 2021), suggesting that interstellar chemistry is not in thermodynamic equilibrium (van Hemert & van Dishoeck 2008). The abundance ratios of C_4H to $c\text{-}C_3H_2$ may give us unique information on the physics and chemistry of hydrocarbon molecules. The distribution of such small unsaturated hydrocarbon molecules in cold cores is important for understanding the formation of other organic molecules. However, there is a paucity of studies about the abundances as well as spatial distributions of C_4H and $c\text{-}C_3H_2$ in cold cores. To further understand the relationship between C_4H and $c\text{-}C_3H_2$, mapping surveys that consider sources with varying C_4H to $c\text{-}C_3H_2$ abundances are necessary.

As a good dense gas tracer, $H^{13}CO^+$ 1–0 is used to investigate the location of cold cores (Artur de la Villarmois et al. 2018). In this work, we investigated the spatial distributions and relative abundances of C_4H , $c\text{-}C_3H_2$, and $H^{13}CO^+$ toward the 19 cold cores. A comprehensive survey of these cores was conducted to determine the connection between C_4H and $c\text{-}C_3H_2$ in these sources. The organization of this paper is as follows. In Section 2, we describe the mapping observations and data reduction. In Section 3, we show the results of our observations. The discussions are presented in Section 4 and a summary is given in Section 5.

2. OBSERVATION AND DATA REDUCTION

The on-the-fly (OTF) mapping observations of a sample of 19 Planck Cold Dust Clumps as cold dust clumps as cold molecular cores, which were selected with strong CO 1–0 emission (Wu et al. 2012), were made with the IRAM 30m telescope on Pico Veleta, Spain, in 2020 September (project number: 016-20, PI: Shu Liu). The data were taken with the 3 mm (E0) band of the Eight Mixer Receiver and the fast Fourier transform spectrometers backend covering two intermediate frequencies with a 2 GHz bandwidth and 48.8 kHz spectral resolution in dual polarization. The beam size of the IRAM 30m telescope is $\sim 24''$ at 85 GHz. The typical system temperatures were around 150 K in the 3 mm band. Pointing was checked every 2 hours with nearby strong quasars. Focus was checked and corrected at the beginning of each run and during sunsets/sunrises. The antenna temperature (T_A^*) was converted to the main beam brightness temperature (T_{mb}), using $T_{mb} = T_A^* \cdot F_{eff} / B_{eff}$, where the forward efficiency F_{eff} is 0.95 and beam efficiency B_{eff} is 0.81 for the 3 mm band. The pixel size of the final regridded maps was $9''$.

C_4H (9–8), $c\text{-}C_3H_2$ ($J_{Ka,Kb}=2_{1,2}-1_{0,1}$) (hereafter $c\text{-}C_3H_2$ 2–1) and $H^{13}CO^+$ ($J=1-0$) (hereafter $H^{13}CO^+$ 1–0) lines were included in the observations. Detailed information on the physical parameters of the molecular lines was obtained from the Cologne Database for Molecular Spectroscopy (CDMS)¹ (Müller et al. 2005) and is listed in Table 1. All data processing was conducted for the regridded maps using the CLASS package, which is a part of the GILDAS² software. For each line observed for each source, we first took a quick look at the velocity ranges in the spectral emission region. These velocity ranges were used as ‘mask’ with ‘set window’ in CLASS when the first-order baseline was removed. Then we used ‘print area’ in CLASS to get the velocity-integrated fluxes for each pixel, which provided spatial distribution maps for each line.

Since C_4H 9–8 ($J=19/2-17/2$) is strongly blended with C_4H 9–8 ($J=19/2-19/2$), which cannot be separated due to line broadening, both of them are marked as C_4H 9–8 ($J=19/2-17/2$) later in this paper. There similar cases are for C_4H 9–8 ($J=17/2-15/2$) and C_4H 9–8 ($J=17/2-17/2$). The information of the observations for each source is shown in Table 2.

3. RESULTS

With the mapping observations of 19 cold cores, $H^{13}CO^+$ 1–0 was detected in all sources. $c\text{-}C_3H_2$ 2–1 emission was detected in 18 sources, except for G008.52+21. The emission of C_4H 9–8 ($J=19/2-17/2$) and C_4H 9–8 ($J=17/2-15/2$) was detected in 13 sources while remaining undetected in G003.73+16, G006.32+20, G006.41+20, G008.52+21, G031.44+04, and G032.93+02 (see Table 3).

3.1. Spatial distribution of C_4H , $c\text{-}C_3H_2$ and $H^{13}CO^+$ lines

Considering the comparable weakness of the individual signals of C_4H 9–8 ($J=19/2-17/2$) and C_4H 9–8 ($J=17/2-15/2$), along with the nearly identical Einstein coefficients and upper-level energies, combining them into one total velocity-integrated intensity is a reasonable approach, which offers a higher fidelity for analyzing the C_4H distribution

¹ <https://cdms.astro.uni-koeln.de/classic>

² <http://www.iram.fr/IRAMFR/GILDAS>

compared with one single line. The averaged value of the two C₄H 9–8 lines will be used for the discussion of the spatial distribution of C₄H.

The velocity-integrated intensity maps of C₄H 9–8 (magenta contours), *c*-C₃H₂ 2–1 (gray scale and blue contours) and H¹³CO⁺ 1–0 (green contours) of six sources are shown in Figure 1 (G001.38+20, G001.84+16, G006.04+36, G021.20+04, and G021.66+03) and Figure 2 (G032.93+22), while other sources are displayed in Figure A1. Two velocity components with different spatial distributions derived from a velocity-integrated map were found in G032.93+22. The two velocity ranges were from 10.8 to 12.2 km s⁻¹ and 12.2 to 13.4 km s⁻¹, respectively, for deriving velocity-integrated maps (see Figure 2).

The spatial distribution information of C₄H 9–8, *c*-C₃H₂ 2–1 and H¹³CO⁺ 1–0 for each source is listed in Table 3. C₄H 9–8 spatial distributions could be clearly found in 10 out of 13 sources. However, our current sensitivity and angular resolution are insufficient to unveil the spatial distributions of C₄H 9–8 in the remaining three sources (G001.84+16, G007.14+05, and G021.20+04). *c*-C₃H₂ 2–1 was only marginally detected in G006.32+20 and G006.41+20, while clear spatial distribution could be found in the other 16 sources. H¹³CO⁺ 1–0 emission could be resolved in all 19 sources.

Among the 13 sources with detection of C₄H 9–8, different spatial distribution between C₄H 9–8 and *c*-C₃H₂ 2–1 could be found in 4 sources (G001.84+16, G007.14+05, G021.20+04, and G021.66+03). Even though C₄H 9–8 in G007.14+05 and G021.20+04 could not be resolved mainly due to weak emission, a clear spatial offset between the peak of C₄H 9–8 and *c*-C₃H₂ 2–1 could be found. Different spatial distributions between C₄H 9–8 and *c*-C₃H₂ 2–1 could not be found in the other 9 sources (G001.38+20, G006.04+36, G008.67+22, G025.48+06, G026.85+06, G028.45-06, G028.71+03, G030.78+05, and G058.16+03).

Notes for individual sources with useful spatial information are presented below:

G001.38 + 20: A 220'' × 220'' map of C₄H 9–8, *c*-C₃H₂ 2–1 and H¹³CO⁺ 1–0 was obtained. Strong emissions of *c*-C₃H₂ 2–1 and H¹³CO⁺ 1–0 were detected with similar spatial distribution, which shows a banded structure extended over 200'' in the east-to-west direction. The three lines peak at the same position approximately at (-90'', 10'').

G001.84 + 16: The OTF mode was used to cover 120'' × 120'' for C₄H 9–8, *c*-C₃H₂ 2–1 and H¹³CO⁺ 1–0. Both *c*-C₃H₂ 2–1 and H¹³CO⁺ 1–0 were detected and were seen with significantly different spatial distributions. *c*-C₃H₂ 2–1 distributes in a north-to-south direction at the east of the mapping area, extending over 120'', while H¹³CO⁺ 1–0 shows a northwest-to-southeast direction distribution. Weak C₄H 9–8 emission is mainly located at the northeast of the mapping area.

G006.04 + 36: The mapping size of C₄H 9–8, *c*-C₃H₂ 2–1 and H¹³CO⁺ 1–0 is 240'' × 240''. Two strong *c*-C₃H₂ 2–1 components were evident, with one centered at about (-50'', -50'') and the other at (0'', 50''). In contrast, two H¹³CO⁺ 1–0 components were observed, one predominantly centered around (-150'', -130'') without *c*-C₃H₂ 2–1 emission, and the other centered at about (-50'', -80'') in close proximity to *c*-C₃H₂ 2–1 emission. No H¹³CO⁺ 1–0 was detected near the component centered at about (0'', 50''), where both *c*-C₃H₂ 2–1 and C₄H 9–8 were detected. The three components present different properties based on the emission of these three lines.

G021.20 + 04: The mapping size of C₄H 9–8, *c*-C₃H₂ 2–1 and H¹³CO⁺ 1–0 is 220'' × 100''. All three lines were detected, showing different spatial distributions. Strong *c*-C₃H₂ 2–1 and H¹³CO⁺ 1–0 emissions exhibit a north-to-south distribution centered at about (30'', 0''). The emission peaks of all three lines are different. The peak coordinates of *c*-C₃H₂ 2–1 and H¹³CO⁺ 1–0 are about (30'', 0''). C₄H 9–8 shows two peaks in the northeast and southwest directions of *c*-C₃H₂ 2–1 approximately at (40'', 25'') and (25'', -20'').

G021.66 + 03: A 220'' × 220'' size map of C₄H 9–8, *c*-C₃H₂ 2–1 and H¹³CO⁺ 1–0 was obtained. No clear difference in the spatial distributions between *c*-C₃H₂ 2–1 and H¹³CO⁺ 1–0 was found, with a semielliptical distribution in the north-to-south direction. The *c*-C₃H₂ 2–1 and H¹³CO⁺ 1–0 emission peak is at about (-5'', 45''). The C₄H 9–8 emission presents a slightly different spatial distribution from that of *c*-C₃H₂ 2–1 and H¹³CO⁺ 1–0.

G032.93 + 22: Two velocity components with different spatial distributions were found for both *c*-C₃H₂ 2–1 and H¹³CO⁺ 1–0 (see Figure 1), while C₄H 9–8 was not detected in the velocity-integrated map. The spatial distribution of *c*-C₃H₂ 2–1 is similar to that of H¹³CO⁺ 1–0 for each velocity component. After being spatially averaged with several pixels, C₄H 9–8 was detected for both velocity components (see Figure 2).

3.2. Column densities and relative abundances

Based on the velocity-integrated maps of C₄H 9–8, *c*-C₃H₂ 2–1 and H¹³CO⁺ 1–0, there was more than one core in some sources, so 25 regions from the 19 mapping sources were selected to calculate the relative abundance of the three molecules. The spatially averaged spectra of these three lines were used to derive velocity-integrated intensities with

a single-component Gaussian fitting. The regions used for obtaining the spatially averaged spectra are marked with yellow boxes, while black boxes are also used if the second core is used in one map.

Both $c\text{-C}_3\text{H}_2$ 2–1 and H^{13}CO^+ 1–0 were detected in 25 regions. C_4H 9–8 ($J=19/2-17/2$) and C_4H 9–8 ($J=17/2-15/2$) emission was detected in 21 regions except for G006.32+20 (yellow), G006.41+20 (yellow), G008.52+21 (yellow), and G032.93+02 (black). Detailed information on the spectra obtained from the 25 regions is shown in Table 5, including source names, molecular line names, velocity-integrated intensities, FWHM and peak temperatures. The strongest emissions of C_4H 9–8 ($J=19/2-17/2$) and C_4H 9–8 ($J=17/2-15/2$) were observed in G028.71+03 (yellow) with integrated intensities of 0.93 ± 0.03 and 0.88 ± 0.02 K km s $^{-1}$, respectively. Meanwhile, the strongest emissions of $c\text{-C}_3\text{H}_2$ 2–1 and H^{13}CO^+ 1–0 were identified in G030.78+05 (yellow) with integrated intensities of 2.75 ± 0.02 and 2.12 ± 0.03 K km s $^{-1}$, respectively.

For sources where C_4H 9–8 was not detected, 3σ upper limits for $\int T_{\text{mb}} dv$ were calculated:

$$\int T_{\text{mb}} dv = 3rms\sqrt{\delta v \cdot \Delta v} \text{ (K km s}^{-1}\text{)}, \quad (1)$$

where δv is the velocity resolution, Δv is the line width in km s $^{-1}$, and rms is the root mean square value per channel of the spectrum.

Even though local thermodynamic equilibrium (LTE) is hard to be reached for molecules, such as C_4H and $c\text{-C}_3\text{H}_2$, with dipole moment higher than that of CO, LTE assumption is still a reasonable approximation for deriving column density with only one transition of each molecule. Assuming LTE and that all three lines are optically thin, the formula for calculating the column density of these three molecules can be given by

$$N_{\text{tot}} = \frac{8\pi k\nu^2}{hc^3 A_{ul}} \frac{Q(T_{\text{ex}})}{g_u} e^{E_u/kT_{\text{ex}}} \int T_{\text{mb}} dv \text{ (cm}^{-2}\text{)} \quad (2)$$

where k is the Boltzmann constant, ν is the frequency of the molecular spectral line transition, h is the Planck constant, c is the speed of light, A_{ul} is the Einstein emission coefficient, g_u is the upper-level degeneracy, and E_u is the energy of the upper level above the ground state. The frequency ν , g_u , A_{ul} , and E_u for six emission lines (C_4H 9–8 ($J=19/2-17/2$), C_4H 9–8 ($J=19/2-19/2$), C_4H 9–8 ($J=17/2-15/2$), C_4H 9–8 ($J=17/2-17/2$), $c\text{-C}_3\text{H}_2$ ($J_{Ka,Kb}=2_{1,2}-1_{0,1}$), H^{13}CO^+ ($J=1-0$)) were taken from the CDMS. $Q(T_{\text{ex}})$ is the partition function, which is depends on the excitation temperature T_{ex} . Since all the sources were selected from cold cores, the excitation temperature $T_{\text{ex}} = 9.375$ K was taken for the calculations in this work. Detailed information is shown in Table 1 from the CDMS.

The frequency difference among C_4H 9–8 ($J=19/2-17/2$) and C_4H 9–8 ($J=19/2-19/2$) as well as C_4H 9–8 ($J=17/2-15/2$) and C_4H 9–8 ($J=17/2-17/2$) is very small, which leads to the blending of these lines. We calculate the column densities of C_4H with

$$N_{\text{tot}} = \frac{8\pi k\nu^2}{hc^3} \frac{Q(T_{\text{ex}})}{A_{ul_1}g_{u_1} + A_{ul_2}g_{u_2}} e^{E_u/kT_{\text{ex}}} \int T_{\text{mb}} dv \text{ (cm}^{-2}\text{)} \quad (3)$$

where A_{ul_1} , g_{u_1} , and A_{ul_2} , g_{u_2} are the values corresponding to the two blended lines, respectively. Since the difference in E_u between the two blended molecular lines is also very small, we take the E_u values of C_4H 9–8 ($J=19/2-17/2$) and C_4H 9–8 ($J=17/2-15/2$).

The relative abundances of C_4H and $c\text{-C}_3\text{H}_2$ to H^{13}CO^+ , and the column densities of the three molecules are presented in Table 6. In this table, columns (2)–(4) present the derived column densities of the three molecules, while Column (5)–(7) display their relative abundances.

The derived column densities of the three molecules are in Columns (2)–(4) and the relative abundances in Columns (5)–(7). The abundance ratio of C_4H to $c\text{-C}_3\text{H}_2$ ranges from 0.34 ± 0.09 in G032.93+02 (yellow) to 4.65 ± 0.53 in G008.67+22 (yellow) (see Table 6).

4. DISCUSSION

With similar Einstein A coefficients and upper-level energies (see Table 1), $c\text{-C}_3\text{H}_2$ 2–1 and H^{13}CO^+ 1–0 do represent the abundances of $c\text{-C}_3\text{H}_2$ and H^{13}CO^+ molecules instead of the excitation conditions caused by volume densities and the kinetic temperature of molecular hydrogen. On the other hand, given a higher $E_u \sim 20.5$ K than that of $c\text{-C}_3\text{H}_2$ 2–1 (~ 6.4 K) and H^{13}CO^+ 1–0 (~ 4.2 K), the excitation of C_4H 9–8 demands a high kinetic temperature. Significantly different spatial distributions between $c\text{-C}_3\text{H}_2$ 2–1 and H^{13}CO^+ 1–0 are seen in several sources (G001.84+16,

G006.04+36, G006.32+20, G006.41+20, and G008.52+21), while no clear difference can be found in other sources. Such differences indicate that the enhancement of *c*-C₃H₂ can exist even in the cold cores. On the other hand, the absence of C₄H in some cores can be explained by their low kinetic temperatures of molecular gas.

The detected abundances of C₄H and *c*-C₃H₂ relative to those of H¹³CO⁺ in the 25 regions are plotted in Figure 3. Only upper limits of C₄H column densities are obtained in four regions, while *c*-C₃H₂ and H¹³CO⁺ column densities are obtained in all 25 regions. The detection of C₄H and C₃H₂ in different cores may vary due to the diverse chemical reaction pathways associated with these two molecules, as well as variations in excitation temperatures among different sources. The abundance ratio of C₄H/H¹³CO⁺ varies from about 3 to 50, while it is about 2 to 18 for the ratio of *c*-C₃H₂/H¹³CO⁺. Even though C₄H 9–8 lines are normally weaker than those of *c*-C₃H₂ 2–1 in these regions, the relative abundances of C₄H are comparable or slightly higher than those of *c*-C₃H₂ in most of them (see Figure 4), which is caused by the higher energy levels of C₄H than those of *c*-C₃H₂. Higher abundance of C₄H than that of *c*-C₃H₂ were also seen in the “starless” core L1521F (Takakuwa et al. 2011), Orion Bar PDR (Cuadrado et al. 2015), and four low-mass molecular outflow sources (Zhang et al. 2021). Different excitation conditions for molecules with different dipole moments and critical densities can cause uncertainties in estimating column densities and relative abundances with only one transition for each molecule. If the excitation temperature of *c*-C₃H₂ is lower than that of C₄H, it will result in a decrement in column density of *c*-C₃H₂ and an increment in the abundance ratio of C₄H to *c*-C₃H₂. Further observations of multiple transitions will help us to better determine the abundance of each molecule. For example, combination of C₄H 5–4 lines with existing 9–8 lines, and combination of *c*-C₃H₂ 3–2 with 2–1, can be used to derive a more accurate relative abundance of *c*-C₃H₂ and C₄H. Improving the signal-to-noise ratio of such a weak emission can also be necessary to derive an accurate abundance ratio.

A very weak trend of increment of C₄H and/or H¹³CO⁺ with an increasing *c*-C₃H₂/H¹³CO⁺ abundance ratio is observed. The result is $lg(C_4H/H^{13}CO^+) = 3.35lg(c-C_3H_2/H^{13}CO^+) - 2.20$, with a correlation coefficient of 0.46, using least-square fitting (see Figure 3). The four upper limits are not used for the fitting. Even though the detected C₄H 9–8 emissions are mainly associated with *c*-C₃H₂ 2–1 emission based on the mapping results, it seems that there is no strong astrochemical connection between C₄H and *c*-C₃H₂ molecules in cold cores. This is supported by the observed large variation in the C₄H/*c*-C₃H₂ abundance ratio and the astrochemical modeling results (Harada & Herbst 2008; Loison et al. 2017). Based on the Kinetic Database for Astrochemistry network, C₄H was thought to be formed through some routes for the C_nH family from n=2 to n=10 (Remijan et al. 2023). C₄H can also be formed through the reaction of C with *l*-C₃H₂ (Loison et al. 2014), which is less abundant than *c*-C₃H₂ in molecular clouds. On the other hand, C₄H can be destroyed by the radiative absorption of an electron to form C₄H[−] (Harada & Herbst 2008; Gianturco et al. 2016). *c*-C₃H₂ was thought to be formed by the dissociative recombination of C₃H₃⁺ (Herbst et al. 1984; Smith & Adams 1987; Park et al. 2006), with *c*-C₃H₃⁺+e[−] to produce *c*-C₃H₂ and H. Another pathway for the formation of *c*-C₃H₂ involves the reaction between *l*-C₃H₂ and H (Loison et al. 2017), which can result in a weak astrochemical connection between *c*-C₃H₂ and C₄H. The efficient destruction pathway for *c*-C₃H₂ involves the reaction with O, producing HC₃O in dense molecular clouds (Loison et al. 2017). The comparable abundances of C₄H and *c*-C₃H₂ found in these sources (see Table 6), should be considered in further astrochemical network pathways for these two molecules in cold molecular cores. However, due to the limited observational results of C₄H and *c*-C₃H₂ in varying conditions of the ISM, it is hard to make a conclusion about the dominant chemical network of these two molecules. The widely existing *c*-C₃H₂ and C₄H in cold molecular cores provide the building blocks for the formation of large organic molecules in the ISM. Further high-resolution observations with millimeter interferometers will be useful to obtain a more comprehensive understanding of C₄H and *c*-C₃H₂ chemistry in molecular clouds.

5. SUMMARY

With the mapping observations of 19 cold molecular cores for C₄H (N=9-8 J=19/2-17/2, N=9-8 J=19/2-19/2, N=9-8 J=17/2-15/2, N=9-8 J=17/2-17/2), *c*-C₃H₂ ($J_{Ka,Kb}=2_{1,2}-1_{0,1}$) and H¹³CO⁺ (J=1–0), using the IRAM 30m telescope, the main results are:

1. H¹³CO⁺ 1–0 emission was detected in all 19 sources, while *c*-C₃H₂ 2–1 was detected in 18 sources and C₄H 9–8 was detected in 13 sources. The high detection rate of *c*-C₃H₂ and C₄H lines indicates that such unsaturated hydrocarbon molecules can be formed in cold core or even earlier phases.

2. The emission of *c*-C₃H₂ 2–1 and H¹³CO⁺ 1–0, with similar Einstein A coefficients and upper-level energies, in some sources presents different spatial distributions, which implies that *c*-C₃H₂ has a distinct chemistry compared to H¹³CO⁺.

3. The abundance ratio of C_4H to $c-C_3H_2$ spans a wide range from 0.34 ± 0.09 in G032.93+02 to 4.65 ± 0.50 in G008.67+22.

4. The maximum abundance ratio of C_4H to $H^{13}CO^+$ is 51.48 ± 2.90 in G028.71+03, and the maximum abundance ratio of $c-C_3H_2$ to $H^{13}CO^+$ is 16.48 ± 3.50 in G007.14+05.

5. Only a very weak trend between the $C_4H/H^{13}CO^+$ and $c-C_3H_2/H^{13}CO^+$ abundance ratio was found, which is consistent with the astrochemical networks of C_4H and $c-C_3H_2$ in which there is no close connection between these two molecules.

1 This work has been supported by the University Annual Scientific Research Plan of Anhui Province (No.
2 2023AH030052, No. 2022AH010013), Zhejiang Lab Open Research Project (No. K2022PE0AB01), the National
3 Natural Science Foundation of China grants 11988101, the China Manned Space Program through its Space Appli-
4 cation System, the science research grants from the China Manned Space Project with numbers CMS-CSST grant
5 and Cultivation Project for FAST Scientific Payoff and Research Achievement of CAMS-CAS. This study is based on
6 observations carried out under project 016-12 with the IRAM 30m telescope. IRAM is supported by INSU/CNRS
7 (France), MPG (Germany) and IGN (Spain).

REFERENCES

- Artur de la Villarmois, E., Kristensen, L. E., Jørgensen, J. K., et al. 2018, *A&A*, 614, A26.
doi:10.1051/0004-6361/201731603
- Bell, M. B., Matthews, H. E., & Sears, T. J. 1983, *A&A*, 127, 241
- Cuadrado, S., Goicoechea, J. R., Pilleri, P., et al. 2015, *A&A*, 575, A82. doi:10.1051/0004-6361/201524003
- Fossé, D., Cernicharo, J., Gerin, M., et al. 2001, *ApJ*, 552, 168. doi:10.1086/320471
- Guelin, M., Green, S., & Thaddeus, P. 1978, *ApJL*, 224, L27. doi:10.1086/182751
- Gottlieb, C. A., Vrtilek, J. M., Gottlieb, E. W., et al. 1985, *ApJL*, 294, L55. doi:10.1086/184508
- Gianturco, F. A., Grassi, T., & Wester, R. 2016, *Journal of Physics B Atomic Molecular Physics*, 49, 204003. doi:10.1088/0953-4075/49/20/204003
- Herbst, E., Adams, N. G., & Smith, D. 1984, *ApJ*, 285, 618. doi:10.1086/162538
- Harada, N. & Herbst, E. 2008, *ApJ*, 685, 272. doi:10.1086/590468
- Irvine, W. M., Hoglund, B., Friberg, P., et al. 1981, *ApJL*, 248, L113. doi:10.1086/183637
- Loison, J.-C., Wakelam, V., Hickson, K. M., et al. 2014, *MNRAS*, 437, 930. doi:10.1093/mnras/stt1956
- Loison, J.-C., Agúndez, M., Wakelam, V., et al. 2017, *MNRAS*, 470, 4075. doi:10.1093/mnras/stx1265
- Matthews, H. E. & Irvine, W. M. 1985, *ApJL*, 298, L61. doi:10.1086/184567
- Madden, S. C., Irvine, W. M., Matthews, H. E., et al. 1989, *AJ*, 97, 1403. doi:10.1086/115081
- Müller H. S. P., Schlöder F., Stutzki J., Winnewisser G., 2005, *JMoSt*, 742, 215. doi:10.1016/j.molstruc.2005.01.027
- Park, I. H., Wakelam, V., & Herbst, E. 2006, *A&A*, 449, 631. doi:10.1051/0004-6361:20054420
- Pety, J., Gratier, P., Guzmán, V., et al. 2012, *A&A*, 548, A68. doi:10.1051/0004-6361/201220062
- Remijan, A., Scolati, H. N., Burkhardt, A. M., et al. 2023, *ApJL*, 944, L45. doi:10.3847/2041-8213/acb648
- Smith, D. & Adams, N. G. 1987, *International Journal of Mass Spectrometry and Ion Processes*, 76, 307. doi:10.1016/0168-1176(87)83035-5
- Sakai, N., Sakai, T., Hirota, T., et al. 2010, *ApJ*, 722, 1633. doi:10.1088/0004-637X/722/2/1633
- Tucker, K. D., Kutner, M. L., & Thaddeus, P. 1974, *ApJL*, 193, L115. doi:10.1086/181646
- Thaddeus, P., Vrtilek, J. M., & Gottlieb, C. A. 1985, *ApJL*, 299, L63. doi:10.1086/184581
- Takakuwa, S., Ohashi, N., & Aikawa, Y. 2011, *ApJ*, 728, 101. doi:10.1088/0004-637X/728/2/101
- van Hemert, M. C. & van Dishoeck, E. F. 2008, *Chemical Physics*, 343, 292. doi:10.1016/j.chemphys.2007.08.011
- Wu, Y., Liu, T., Meng, F., et al. 2012, *ApJ*, 756, 76. doi:10.1088/0004-637X/756/1/76
- Yamamoto, S., Saito, S., Guelin, M., et al. 1987, *ApJL*, 323, L149. doi:10.1086/185076
- Zhang, C., Wu, Y., Liu, X.-C., et al. 2021, *A&A*, 648, A83. doi:10.1051/0004-6361/202039110

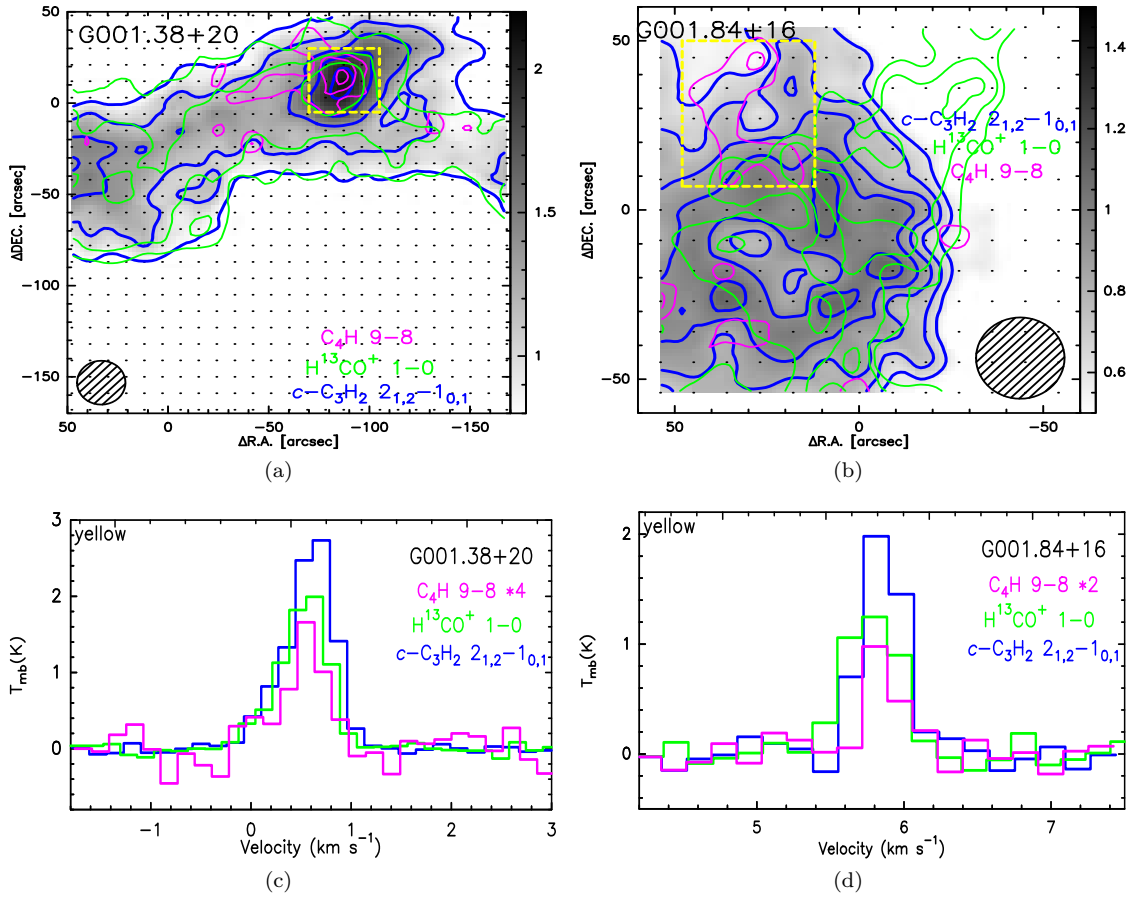
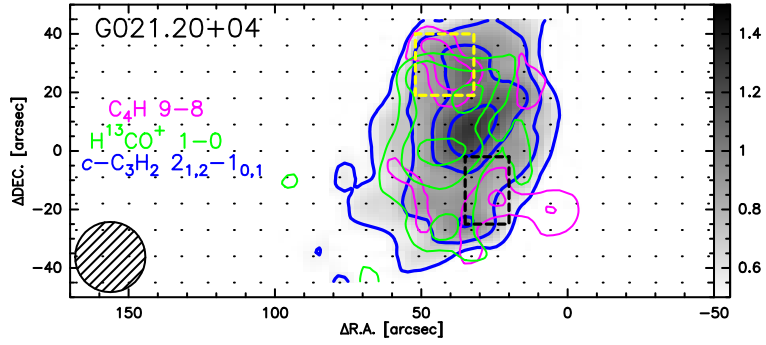
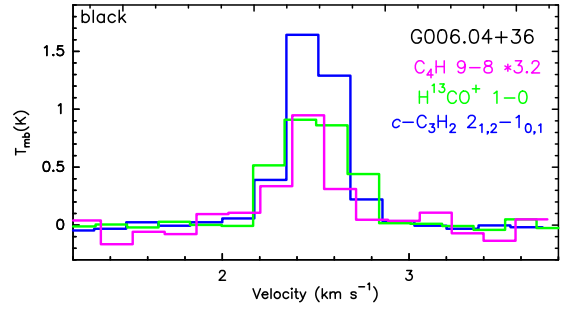
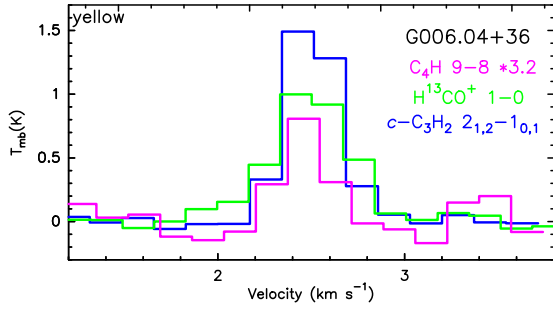
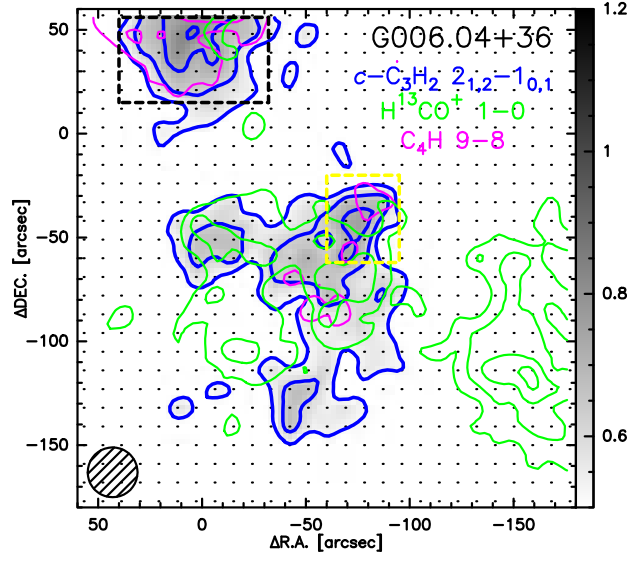


Figure 1. The velocity integrated maps and spatial averaged spectra of C₄H 9-8, *c*-C₃H₂ 2-1 and H¹³CO⁺ 1-0. The source names are presented in the maps and spectra. The gray scale color at the right is in units of K km s⁻¹. (a): The velocity integrated intensity maps for C₄H 9-8 (magenta contours), *c*-C₃H₂ 2-1 (blue contours) and H¹³CO⁺ 1-0 (green contours) of G001.38+20. (b): The same as Figure 1(a) but for G001.84+16. (c): Spectra of C₄H at 85672.5793 MHz, *c*-C₃H₂ at 85338.8940 MHz and H¹³CO⁺ at 86754.2884 MHz in the yellow box of G001.38+20. (d): The same as Figure 1(c) but for G001.84+16. The detailed mapping information of all sources for C₄H 9-8, *c*-C₃H₂ 2-1 and H¹³CO⁺ 1-0 are listed in Table 4.



gridline

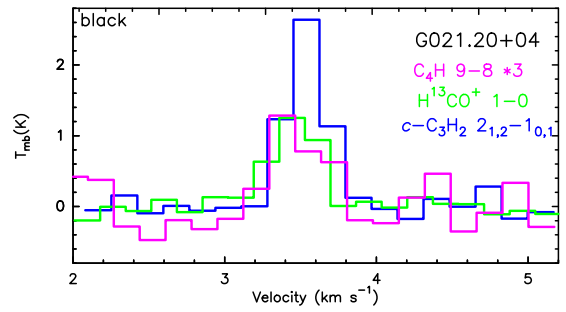
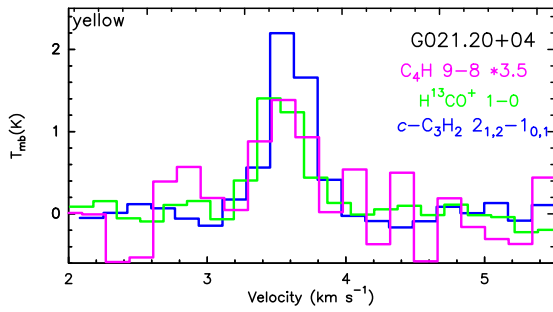


Figure 1. Continued.

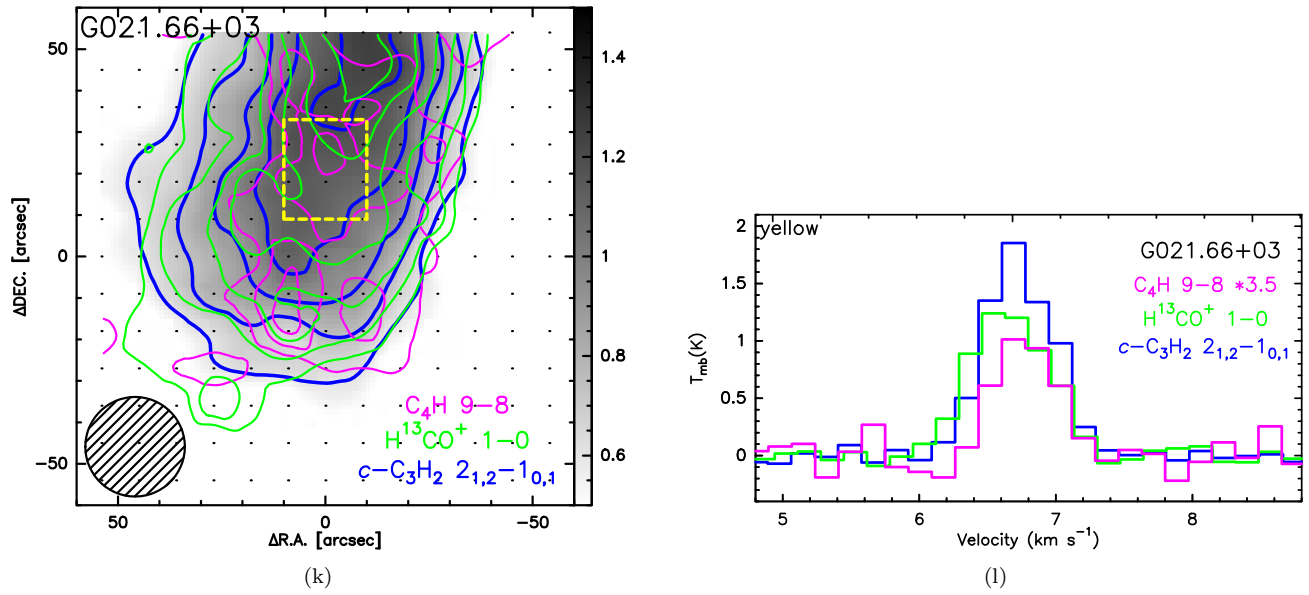


Figure 1. Continued.

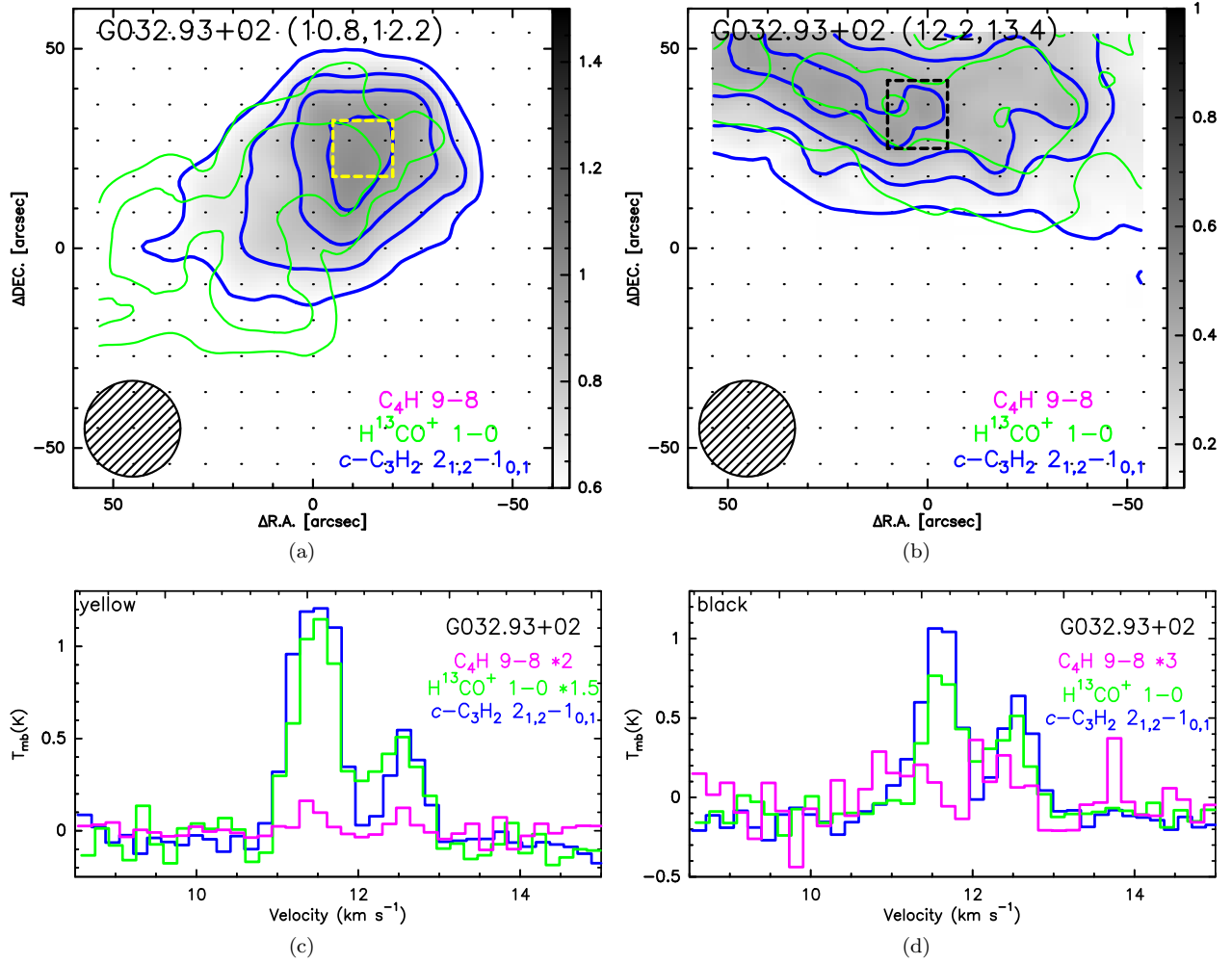


Figure 2. (a): The velocity integrated intensity maps for $c\text{-C}_3\text{H}_2$ 2-1 (blue contour) and H^{13}CO^+ 1-0 (green contour) of G032.93+22, velocity integral range from 10.8 to 12.2. (b): The velocity integrated intensity maps for $c\text{-C}_3\text{H}_2$ 2-1 and H^{13}CO^+ 1-0 of G032.93+22, velocity integral range from 12.2 to 13.4. (c): Spectra of C_4H at 85672.5793 MHz, $c\text{-C}_3\text{H}_2$ at 85338.8940 MHz and H^{13}CO^+ at 86754.2884 MHz in the yellow box of G032.93+22. (d): Spectra of C_4H at 85672.5793 MHz, $c\text{-C}_3\text{H}_2$ at 85338.8940 MHz and H^{13}CO^+ at 86754.2884 MHz in the black box of G032.93+22.

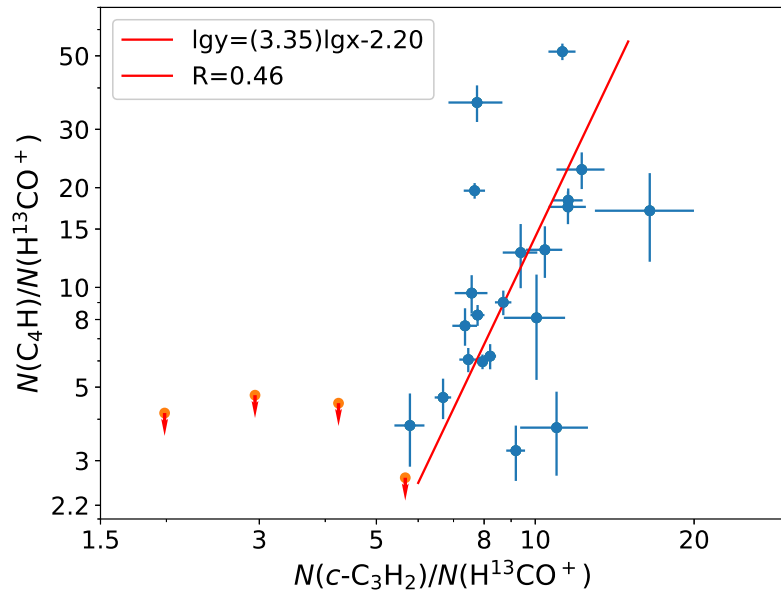


Figure 3. The relation between $c\text{-C}_3\text{H}_2/\text{H}^{13}\text{CO}^+$ and $\text{C}_4\text{H}/\text{H}^{13}\text{CO}^+$ abundance ratio in 25 regions of the 19 sources and the red points are limits of C_4H .

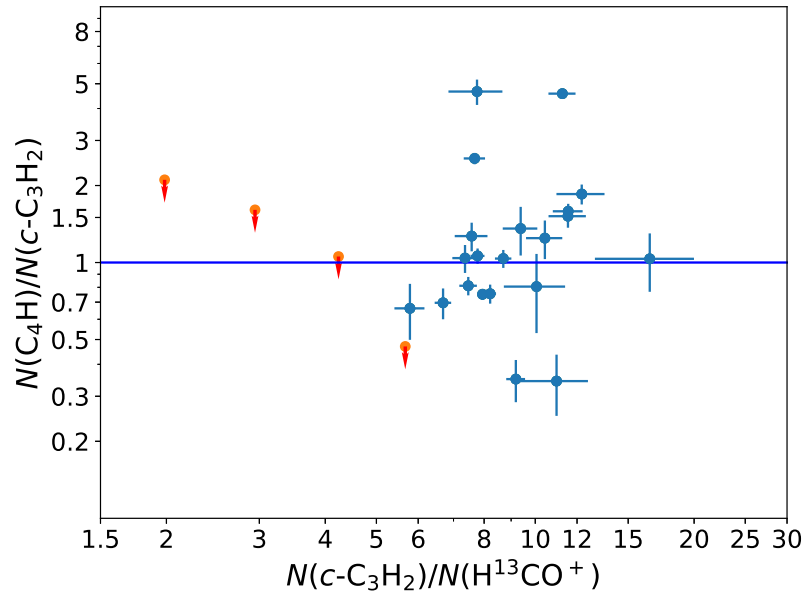


Figure 4. The variation of $\text{C}_4\text{H}/c\text{-C}_3\text{H}_2$ abundance ratio along with $c\text{-C}_3\text{H}_2/\text{H}^{13}\text{CO}^+$ in 25 regions of the 19 sources. The blue line indicates where the $\text{C}_4\text{H}/c\text{-C}_3\text{H}_2$ abundance ratio is unity.

Table 1. Physical parameters of C₄H, *c*-C₃H₂ and H¹³CO⁺.

Molecular	Q _{9.375}	Transition	Freq (MHz)	E_{up} (K)	g_u	A (10 ⁻⁵ s ⁻¹)
C ₄ H	165.5392	N=9-8 J=19/2-17/2	85634.0044	20.561	19	1.5175
	165.5392	N=9-8 J=19/2-19/2	85634.0154	20.561	21	1.5267
	165.5392	N=9-8 J=17/2-15/2	85672.5793	20.563	17	1.5078
	165.5392	N=9-8 J=17/2-17/2	85672.5815	20.563	19	1.5193
<i>c</i> -C ₃ H ₂	72.4028	J=2(1,2)-1(0,1)	85338.8940	6.445	15	2.3221
H ¹³ CO ⁺	4.8522	J=1-0	86754.2884	4.164	3	3.8535

Table 2. Source information and observing parameters.

Source Name	R.A. (hh:mm:ss)	Decl. (dd:mm:ss)	rms (10 ⁻² K)	Mapping Size (")	v_{LSR} (km s ⁻¹)
G001.38+20	16:34:38.06	-15:46:40.7	5.5	220 × 220	0.6
G001.84+16	16:50:12.91	-18:04:22.3	5.2	120 × 120	5.9
G003.73+16	16:55:21.78	-16:43:35.3	6.8	120 × 120	6.1
G006.04+36	15:54:10.81	-02:50:56.3	4.5	240 × 240	2.5
G006.32+20	16:47:40.85	-12:22:03.3	9.4	120 × 120	4.3
G006.41+20	16:47:28.67	-12:13:52.5	7.3	120 × 120	4.4
G007.14+05	17:39:47.47	-19:45:05.1	1.4	100 × 100	10.4
G008.52+21	16:47:48.42	-09:53:09.8	9.7	110 × 110	3.8
G008.67+22	16:47:07.71	-09:35:50.0	7.4	120 × 120	3.6
G021.20+04	18:12:01.72	-08:05:27.7	1.1	220 × 100	3.6
G021.66+03	18:17:06.23	-08:14:35.1	4.7	120 × 120	6.7
G025.48+06	18:15:46.82	-03:45:19.2	1.4	120 × 55	7.7
G026.85+06	18:15:46.82	-03:45:19.2	4.7	240 × 140	7.2
G028.45-06	19:06:09.21	-06:52:51.7	5.5	120 × 120	12.3
G028.71+03	18:29:55.29	-01:58:10.4	5.2	120 × 120	7.5
G030.78+05	18:28:54.49	+00:28:40.0	3.7	120 × 240	8.0
G031.44+04	18:28:54.49	+00:28:40.0	4.8	230 × 110	11.1
G032.93+02	18:41:52.83	+01:13:45.3	4.6	120 × 120	11.5
G058.16+03	18:41:52.83	+01:13:45.3	6.3	120 × 120	9.9

Table 3. C₄H 9-8, *c*-C₃H₂ 2-1 and H¹³CO⁺ 1-0 distribution information.

Source Name	C ₄ H(9-8)		<i>c</i> -C ₃ H ₂ (2-1)		H ¹³ CO ⁺ (1-0)		Difference between C ₄ H(9-8) and <i>c</i> -C ₃ H ₂ (2-1)
	Detection	Clear Feature	Detection	Clear Feature	Detection	Clear Feature	
G001.38+20	✓	✓	✓	✓	✓	✓	...
G001.84+16	✓	...	✓	✓	✓	✓	✓
G003.73+16	✓	✓	✓	✓	...
G006.04+36	✓	✓	✓	✓	✓	✓	...
G006.32+20	✓	...	✓	✓	...
G006.41+20	✓	...	✓	✓	...
G007.14+05	✓	...	✓	✓	✓	✓	✓
G008.52+21	✓	✓	...
G008.67+22	✓	✓	✓	✓	✓	✓	...
G021.20+04	✓	...	✓	✓	✓	✓	✓
G021.66+03	✓	✓	✓	✓	✓	✓	✓
G025.48+06	✓	✓	✓	✓	✓	✓	...
G026.85+06	✓	✓	✓	✓	✓	✓	...
G028.45-06	✓	✓	✓	✓	✓	✓	...
G028.71+03	✓	✓	✓	✓	✓	✓	...
G030.78+05	✓	✓	✓	✓	✓	✓	...
G031.44+04	✓	✓	✓	✓	...
G032.93+02	✓	✓	✓	✓	...
G058.16+03	✓	✓	✓	✓	✓	✓	...

Table 4. Information parameters for map setting of C₄H 9–8, *c*-C₃H₂ 2–1 and H¹³CO⁺ 1–0.

Source name	C ₄ H(9-8)			<i>c</i> -C ₃ H ₂ (2-1)			H ¹³ CO ⁺ (1-0)		
	1 σ	Starting	Step	1 σ	Starting	Step	1 σ	Starting	Step
	K km s ⁻¹	K km s ⁻¹	K km s ⁻¹	K km s ⁻¹	K km s ⁻¹	K km s ⁻¹	K km s ⁻¹	K km s ⁻¹	K km s ⁻¹
G001.38+20	0.07	0.37	0.1	0.05	0.8	0.3	0.05	0.8	0.25
G001.84+16	0.12	0.35	0.13	0.08	0.6	0.11	0.08	0.7	0.1
G003.73+16	0.09	0.07	0.16	0.08	0.07	0.25	0.06
G006.04+36	0.06	0.2	0.08	0.05	0.52	0.1	0.05	0.53	0.1
G006.32+20	0.09	0.07	0.26	0.08	0.07	0.3	0.08
G006.41+20	0.08	0.07	0.25	0.06	0.07	0.2	0.08
G007.14+05	0.07	0.25	0.08	0.09	0.45	0.12	0.09	0.3	0.1
G008.52+21	0.06	0.05	0.05	0.25	0.1
G008.67+22	0.05	0.2	0.08	0.06	0.3	0.08	0.06	0.2	0.06
G021.20+04	0.08	0.35	0.1	0.07	0.55	0.2	0.07	0.5	0.13
G021.66+03	0.06	0.24	0.07	0.05	0.6	0.15	0.05	0.55	0.1
G025.48+06	0.08	0.65	0.12	0.09	0.7	0.15	0.09	0.5	0.12
G026.85+06	0.07	0.36	0.1	0.06	0.4	0.15	0.07	0.5	0.1
G028.45-06	0.06	0.35	0.1	0.06	0.65	0.2	0.07	0.6	0.15
G028.71+03	0.08	0.8	0.18	0.07	0.8	0.12	0.07	0.7	0.08
G030.78+05	0.07	0.45	0.12	0.07	1.7	0.4	0.07	1.5	0.3
G031.44+04	0.08	0.06	0.6	0.15	0.07	0.6	0.1
G032.93+02(yellow)	0.1	0.04	0.6	0.12	0.08	0.5	0.08
G032.93+02(black)	0.1	0.04	0.12	0.1	0.08	0.12	0.08
G058.16+03	0.08	0.3	0.1	0.07	0.45	0.15	0.07	0.4	0.1

Table 5. Observed data of C₄H, *c*-C₃H₂ and H¹³CO⁺.

Source name	Molecular Line		$\int T_{\text{mb}} dv$ (K·km s ⁻¹)	FWHM (km s ⁻¹)	T_{peak} (K)	box color
G001.38+20	C ₄ H	N=9-8 J=19/2-17/2	0.21 ± 0.02	0.46 ± 0.06	0.43	yellow
	C ₄ H	N=9-8 J=17/2-15/2	0.17 ± 0.02	0.42 ± 0.08	0.40	
	<i>c</i> -C ₃ H ₂	J=2(1,2)-1(0,1)	1.59 ± 0.02	0.55 ± 0.01	2.73	
	H ¹³ CO ⁺	J=1-0	1.19 ± 0.03	0.53 ± 0.02	2.01	
G001.84+16	C ₄ H	N=9-8 J=19/2-17/2	0.17 ± 0.03	0.48 ± 0.09	0.34	yellow
	C ₄ H	N=9-8 J=17/2-15/2	0.13 ± 0.02	0.23 ± 0.06	0.55	
	<i>c</i> -C ₃ H ₂	J=2(1,2)-1(0,1)	0.75 ± 0.03	0.33 ± 0.02	2.11	
	H ¹³ CO ⁺	J=1-0	0.60 ± 0.03	0.43 ± 0.03	1.32	
G003.73+16	C ₄ H	N=9-8 J=19/2-17/2	0.05 ± 0.01	0.29 ± 0.09	0.16	yellow
	C ₄ H	N=9-8 J=17/2-15/2	0.03 ± 0.01	0.18 ± 0.22	0.17	
	<i>c</i> -C ₃ H ₂	J=2(1,2)-1(0,1)	0.37 ± 0.01	0.24 ± 0.01	1.42	
	H ¹³ CO ⁺	J=1-0	0.39 ± 0.02	0.39 ± 0.02	0.94	
G006.04+36	C ₄ H	N=9-8 J=19/2-17/2	0.05 ± 0.01	0.20 ± 0.18	0.23	yellow
	C ₄ H	N=9-8 J=17/2-15/2	0.08 ± 0.01	0.29 ± 0.04	0.26	
	<i>c</i> -C ₃ H ₂	J=2(1,2)-1(0,1)	0.58 ± 0.01	0.32 ± 0.01	1.69	
	H ¹³ CO ⁺	J=1-0	0.53 ± 0.02	0.48 ± 0.02	1.05	
G006.04+36	C ₄ H	N=9-8 J=19/2-17/2	0.12 ± 0.01	0.33 ± 0.03	0.35	black
	C ₄ H	N=9-8 J=17/2-15/2	0.09 ± 0.01	0.28 ± 0.03	0.29	
	<i>c</i> -C ₃ H ₂	J=2(1,2)-1(0,1)	0.61 ± 0.01	0.32 ± 0.01	1.81	
	H ¹³ CO ⁺	J=1-0	0.48 ± 0.01	0.46 ± 0.01	1.00	
G006.32+20	C ₄ H	N=9-8 J=19/2-17/2	≤ 0.052	yellow
	C ₄ H	N=9-8 J=17/2-15/2	≤ 0.053	
	<i>c</i> -C ₃ H ₂	J=2(1,2)-1(0,1)	0.31 ± 0.03	0.37 ± 0.05	0.79	
	H ¹³ CO ⁺	J=1-0	0.45 ± 0.05	0.43 ± 0.06	0.98	
G006.41+20	C ₄ H	N=9-8 J=19/2-17/2	≤ 0.045	yellow
	C ₄ H	N=9-8 J=17/2-15/2	≤ 0.049	
	<i>c</i> -C ₃ H ₂	J=2(1,2)-1(0,1)	0.18 ± 0.04	0.61 ± 0.15	0.28	
	H ¹³ CO ⁺	J=1-0	0.38 ± 0.03	0.50 ± 0.06	0.71	
G007.14+05	C ₄ H	N=9-8 J=19/2-17/2	0.11 ± 0.03	0.20 ± 1.88	0.52	yellow
	C ₄ H	N=9-8 J=17/2-15/2	0.15 ± 0.05	0.67 ± 0.20	0.22	
	<i>c</i> -C ₃ H ₂	J=2(1,2)-1(0,1)	0.81 ± 0.09	0.98 ± 0.11	0.77	
	H ¹³ CO ⁺	J=1-0	0.30 ± 0.06	0.46 ± 0.08	0.61	
G007.14+05	C ₄ H	N=9-8 J=19/2-17/2	0.08 ± 0.04	0.53 ± 0.24	0.15	black
	C ₄ H	N=9-8 J=17/2-15/2	0.13 ± 0.06	0.55 ± 0.31	0.23	
	<i>c</i> -C ₃ H ₂	J=2(1,2)-1(0,1)	0.86 ± 0.07	0.70 ± 0.06	1.16	
	H ¹³ CO ⁺	J=1-0	0.52 ± 0.06	0.69 ± 0.09	0.71	
G008.52+21	C ₄ H	N=9-8 J=19/2-17/2	≤ 0.051	yellow
	C ₄ H	N=9-8 J=17/2-15/2	≤ 0.053	
	<i>c</i> -C ₃ H ₂	J=2(1,2)-1(0,1)	0.16 ± 0.05	0.50 ± 0.26	0.29	
	H ¹³ CO ⁺	J=1-0	0.48 ± 0.03	0.35 ± 0.03	1.29	
G008.67+22	C ₄ H	N=9-8 J=19/2-17/2	0.23 ± 0.02	0.26 ± 0.02	0.84	yellow
	C ₄ H	N=9-8 J=17/2-15/2	0.23 ± 0.03	0.31 ± 0.05	0.71	
	<i>c</i> -C ₃ H ₂	J=2(1,2)-1(0,1)	0.31 ± 0.02	0.19 ± 0.04	1.52	
	H ¹³ CO ⁺	J=1-0	0.24 ± 0.02	0.33 ± 0.03	0.69	
G021.20+04	C ₄ H	N=9-8 J=19/2-17/2	0.20 ± 0.06	0.31 ± 0.13	0.62	yellow
	C ₄ H	N=9-8 J=17/2-15/2	0.17 ± 0.05	0.39 ± 0.14	0.41	

Table 5. continued.

Source Name	Molecular Line	$\int T_{\text{mb}} dv$ (K km s ⁻¹)	FWHM (km s ⁻¹)	T_{peak} (K)	Box Color	
G021.20+04	<i>c</i> -C ₃ H ₂	J=2(1,2)-1(0,1)	0.86 ± 0.04	0.34 ± 0.02	2.36	black
	H ¹³ CO ⁺	J=1-0	0.56 ± 0.03	0.35 ± 0.03	1.50	
	C ₄ H	N=9-8 J=19/2-17/2	0.18 ± 0.04	0.37 ± 0.13	0.45	
	C ₄ H	N=9-8 J=17/2-15/2	0.17 ± 0.04	0.39 ± 0.09	0.41	
G021.66+03	<i>c</i> -C ₃ H ₂	J=2(1,2)-1(0,1)	0.88 ± 0.04	0.31 ± 0.02	2.64	yellow
	H ¹³ CO ⁺	J=1-0	0.52 ± 0.03	0.37 ± 0.03	1.32	
	C ₄ H	N=9-8 J=19/2-17/2	0.12 ± 0.02	0.26 ± 0.04	0.43	
	C ₄ H	N=9-8 J=17/2-15/2	0.17 ± 0.02	0.51 ± 0.05	0.31	
G025.48+06	<i>c</i> -C ₃ H ₂	J=2(1,2)-1(0,1)	1.13 ± 0.03	0.59 ± 0.02	1.80	yellow
	H ¹³ CO ⁺	N=1-0	0.93 ± 0.03	0.67 ± 0.02	1.30	
	C ₄ H	N=9-8 J=19/2-17/2	0.42 ± 0.03	0.37 ± 0.03	1.07	
	C ₄ H	N=9-8 J=17/2-15/2	0.35 ± 0.04	0.35 ± 0.04	0.94	
G025.48+06	<i>c</i> -C ₃ H ₂	J=2(1,2)-1(0,1)	1.52 ± 0.04	0.43 ± 0.02	3.28	black
	H ¹³ CO ⁺	J=1-0	0.80 ± 0.05	0.45 ± 0.03	1.67	
	C ₄ H	N=9-8 J=19/2-17/2	0.44 ± 0.04	0.37 ± 0.04	1.12	
	C ₄ H	N=9-8 J=17/2-15/2	0.33 ± 0.05	0.30 ± 0.04	1.03	
G026.85+06	<i>c</i> -C ₃ H ₂	J=2(1,2)-1(0,1)	1.29 ± 0.05	0.41 ± 0.02	2.99	yellow
	H ¹³ CO ⁺	J=1-0	0.65 ± 0.06	0.38 ± 0.05	1.58	
	C ₄ H	N=9-8 J=19/2-17/2	0.28 ± 0.02	0.28 ± 0.02	0.94	
	C ₄ H	N=9-8 J=17/2-15/2	0.24 ± 0.01	0.29 ± 0.02	0.79	
G028.45-06	<i>c</i> -C ₃ H ₂	J=2(1,2)-1(0,1)	0.64 ± 0.02	0.44 ± 0.01	1.39	yellow
	H ¹³ CO ⁺	J=1-0	0.51 ± 0.02	0.54 ± 0.02	0.90	
	C ₄ H	N=9-8 J=19/2-17/2	0.23 ± 0.02	0.53 ± 0.06	0.40	
	C ₄ H	N=9-8 J=17/2-15/2	0.18 ± 0.02	0.46 ± 0.06	0.36	
G028.71+03	<i>c</i> -C ₃ H ₂	J=2(1,2)-1(0,1)	1.21 ± 0.02	0.56 ± 0.01	2.04	yellow
	H ¹³ CO ⁺	J=1-0	0.85 ± 0.03	0.65 ± 0.02	1.22	
	C ₄ H	N=9-8 J=19/2-17/2	0.93 ± 0.03	0.52 ± 0.02	1.68	
	C ₄ H	N=9-8 J=17/2-15/2	0.88 ± 0.02	0.52 ± 0.02	1.60	
G030.78+05	<i>c</i> -C ₃ H ₂	J=2(1,2)-1(0,1)	1.24 ± 0.03	0.99 ± 0.03	1.18	yellow
	H ¹³ CO ⁺	J=1-0	0.67 ± 0.04	0.89 ± 0.05	0.72	
	C ₄ H	N=9-8 J=19/2-17/2	0.33 ± 0.02	0.89 ± 0.07	0.35	
	C ₄ H	N=9-8 J=17/2-15/2	0.33 ± 0.02	0.97 ± 0.08	0.32	
G031.44+04	<i>c</i> -C ₃ H ₂	J=2(1,2)-1(0,1)	2.75 ± 0.02	1.04 ± 0.01	2.49	yellow
	H ¹³ CO ⁺	N=1-0	2.12 ± 0.03	1.22 ± 0.02	1.63	
	C ₄ H	N=9-8 J=19/2-17/2	0.07 ± 0.02	0.55 ± 0.15	0.12	
	C ₄ H	N=9-8 J=17/2-15/2	0.04 ± 0.01	0.19 ± 0.53	0.20	
G032.93+02	<i>c</i> -C ₃ H ₂	J=2(1,2)-1(0,1)	0.99 ± 0.02	0.60 ± 0.01	1.56	yellow
	H ¹³ CO ⁺	J=1-0	0.66 ± 0.02	0.61 ± 0.02	1.01	
	C ₄ H	N=9-8 J=19/2-17/2	0.04 ± 0.02	0.35 ± 0.17	0.12	
	C ₄ H	N=9-8 J=17/2-15/2	0.06 ± 0.02	0.29 ± 0.11	0.18	
G032.93+02	<i>c</i> -C ₃ H ₂	J=2(1,2)-1(0,1)	0.93 ± 0.07	0.65 ± 0.06	1.35	black
	H ¹³ CO ⁺	J=1-0	0.52 ± 0.06	0.63 ± 0.10	0.76	
	C ₄ H	N=9-8 J=19/2-17/2	≤ 0.046	
	C ₄ H	N=9-8 J=17/2-15/2	≤ 0.043	
G032.93+02	<i>c</i> -C ₃ H ₂	J=2(1,2)-1(0,1)	0.60 ± 0.09	0.49 ± 0.09	1.15	black
	H ¹³ CO ⁺	J=1-0	0.64 ± 0.07	1.08 ± 0.13	0.56	

Table 5. continued.

Source Name	Molecular Line		$\int T_{\text{mb}} dv$ (K km s ⁻¹)	FWHM (km s ⁻¹)	T_{peak} (K)	Box Color
G058.16+03	C ₄ H	N=9-8 J=19/2-17/2	0.20 ± 0.03	0.38 ± 0.08	0.48	yellow
	C ₄ H	N=9-8 J=17/2-15/2	0.20 ± 0.02	0.44 ± 0.05	0.43	
	<i>c</i> -C ₃ H ₂	J=2(1,2)-1(0,1)	0.82 ± 0.03	0.37 ± 0.02	2.07	
	H ¹³ CO ⁺	J=1-0	0.44 ± 0.03	0.41 ± 0.04	0.99	
G058.16+03	C ₄ H	N=9-8 J=19/2-17/2	0.16 ± 0.03	0.55 ± 0.14	0.27	black
	C ₄ H	N=9-8 J=17/2-15/2	0.16 ± 0.03	0.61 ± 0.10	0.25	
	<i>c</i> -C ₃ H ₂	J=2(1,2)-1(0,1)	0.97 ± 0.03	0.64 ± 0.02	1.42	
	H ¹³ CO ⁺	J=1-0	0.81 ± 0.04	0.71 ± 0.04	1.06	

Table 6. Column Density and Relative Abundance of C₄H, *c*-C₃H₂ and H¹³CO⁺.

Source Name	$N(\text{C}_4\text{H})$ 10^{12}cm^{-2}	$N(\textit{c}\text{-C}_3\text{H}_2)$ 10^{12}cm^{-2}	$N(\text{H}^{13}\text{CO}^+)$ 10^{12}cm^{-2}	$\frac{N_{\text{C}_4\text{H}}}{N_{\text{H}^{13}\text{CO}^+}}$	$\frac{N_{\textit{c}\text{-C}_3\text{H}_2}}{N_{\text{H}^{13}\text{CO}^+}}$	$\frac{N_{\text{C}_4\text{H}}}{N_{\textit{c}\text{-C}_3\text{H}_2}}$	Box color
G001.38+20	7.04 ± 0.60	9.32 ± 0.13	1.14 ± 0.025	6.20 ± 0.54	8.21 ± 0.21	0.76 ± 0.06	yellow
G001.84+16	5.56 ± 0.67	4.38 ± 0.19	0.58 ± 0.032	9.61 ± 1.27	7.58 ± 0.54	1.27 ± 0.16	yellow
G003.73+16	1.51 ± 0.35	2.16 ± 0.09	0.37 ± 0.020	3.83 ± 0.95	5.78 ± 0.38	0.66 ± 0.16	yellow
G006.04+36	2.37 ± 0.32	3.40 ± 0.07	0.51 ± 0.015	4.65 ± 0.65	6.69 ± 0.24	0.70 ± 0.10	yellow
G006.04+36	3.82 ± 0.26	3.60 ± 0.05	0.46 ± 0.012	8.25 ± 0.60	7.77 ± 0.24	1.06 ± 0.07	black
G006.32+20	≤ 1.94	1.83 ± 0.20	0.43 ± 0.049	≤ 4.47	4.24 ± 0.67	≤ 1.06	yellow
G006.41+20	≤ 1.72	1.07 ± 0.22	0.37 ± 0.030	≤ 4.73	2.94 ± 0.66	≤ 1.61	yellow
G007.14+05	4.90 ± 1.15	4.74 ± 0.50	0.29 ± 0.053	17.04 ± 5.09	16.48 ± 3.5	1.03 ± 0.27	yellow
G007.14+05	4.03 ± 1.34	5.01 ± 0.39	0.50 ± 0.054	8.10 ± 2.84	10.06 ± 1.34	0.80 ± 0.28	black
G008.52+21	≤ 1.91	0.91 ± 0.32	0.46 ± 0.029	≤ 4.18	1.98 ± 0.70	≤ 2.10	yellow
G008.67+22	8.43 ± 0.73	1.81 ± 0.13	0.23 ± 0.021	36.14 ± 4.57	7.77 ± 0.91	4.65 ± 0.50	yellow
G021.20+04	6.87 ± 1.45	5.06 ± 0.23	0.54 ± 0.033	12.74 ± 2.79	9.37 ± 0.71	1.36 ± 0.29	yellow
G021.20+04	6.43 ± 1.06	5.16 ± 0.24	0.50 ± 0.032	12.99 ± 2.30	10.44 ± 0.82	1.24 ± 0.21	black
G021.66+03	5.38 ± 0.42	6.63 ± 0.17	0.89 ± 0.026	6.06 ± 0.51	7.46 ± 0.29	0.81 ± 0.07	yellow
G025.48+06	14.08 ± 0.89	8.88 ± 0.26	0.77 ± 0.045	18.31 ± 1.57	11.55 ± 0.75	1.59 ± 0.11	yellow
G025.48+06	14.02 ± 1.14	7.57 ± 0.29	0.62 ± 0.060	22.68 ± 2.87	12.24 ± 1.28	1.85 ± 0.17	black
G026.85+06	9.62 ± 0.40	3.77 ± 0.11	0.49 ± 0.017	19.59 ± 1.06	7.68 ± 0.36	2.55 ± 0.13	yellow
G028.45-06	7.34 ± 0.58	7.09 ± 0.12	0.81 ± 0.026	9.01 ± 0.77	8.70 ± 0.31	1.04 ± 0.08	yellow
G028.71+03	33.25 ± 0.65	7.27 ± 0.18	0.65 ± 0.035	51.48 ± 2.90	11.25 ± 0.66	4.58 ± 0.14	yellow
G030.78+05	12.10 ± 0.59	16.10 ± 0.13	2.03 ± 0.027	5.97 ± 0.30	7.95 ± 0.13	0.75 ± 0.04	yellow
G031.44+04	2.03 ± 0.38	5.80 ± 0.12	0.63 ± 0.022	3.22 ± 0.61	9.19 ± 0.38	0.35 ± 0.07	yellow
G032.93+02	1.86 ± 0.48	5.42 ± 0.44	0.49 ± 0.060	3.77 ± 1.07	10.97 ± 1.61	0.34 ± 0.09	yellow
G032.93+02	≤ 1.64	3.49 ± 0.53	0.62 ± 0.068	≤ 2.66	5.67 ± 1.07	≤ 0.47	black
G058.16+03	7.31 ± 0.65	4.82 ± 0.20	0.42 ± 0.029	17.50 ± 1.98	11.54 ± 0.94	1.52 ± 0.15	yellow
G058.16+03	5.91 ± 0.72	5.68 ± 0.17	0.77 ± 0.035	7.66 ± 0.99	7.36 ± 0.40	1.04 ± 0.13	black

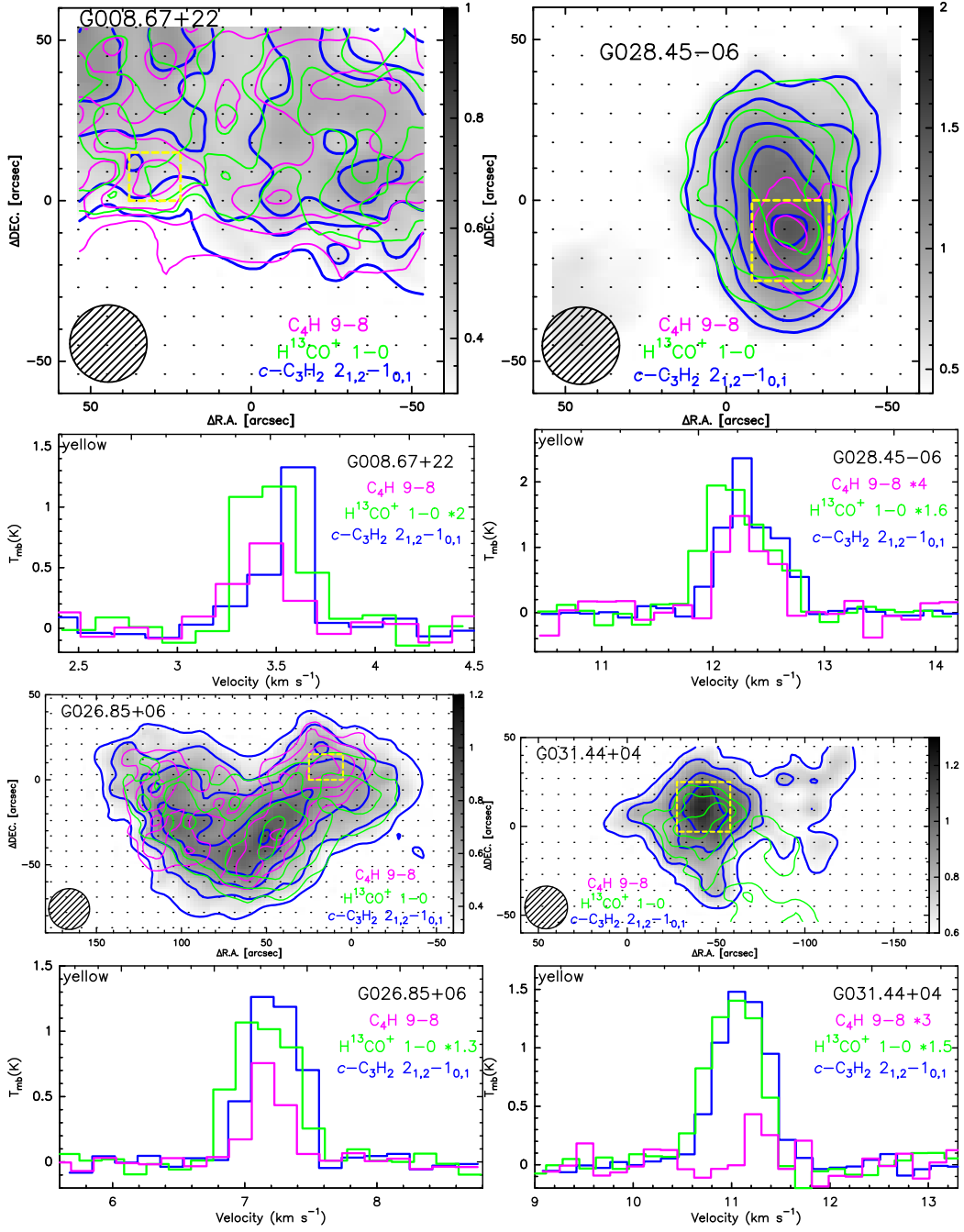


Figure A1. The same as Figure 1 for more sources.

APPENDIX

A. THE SPATIAL DISTRIBUTION MAPS AND SPECTRAL LINES OF ALL SOURCES.

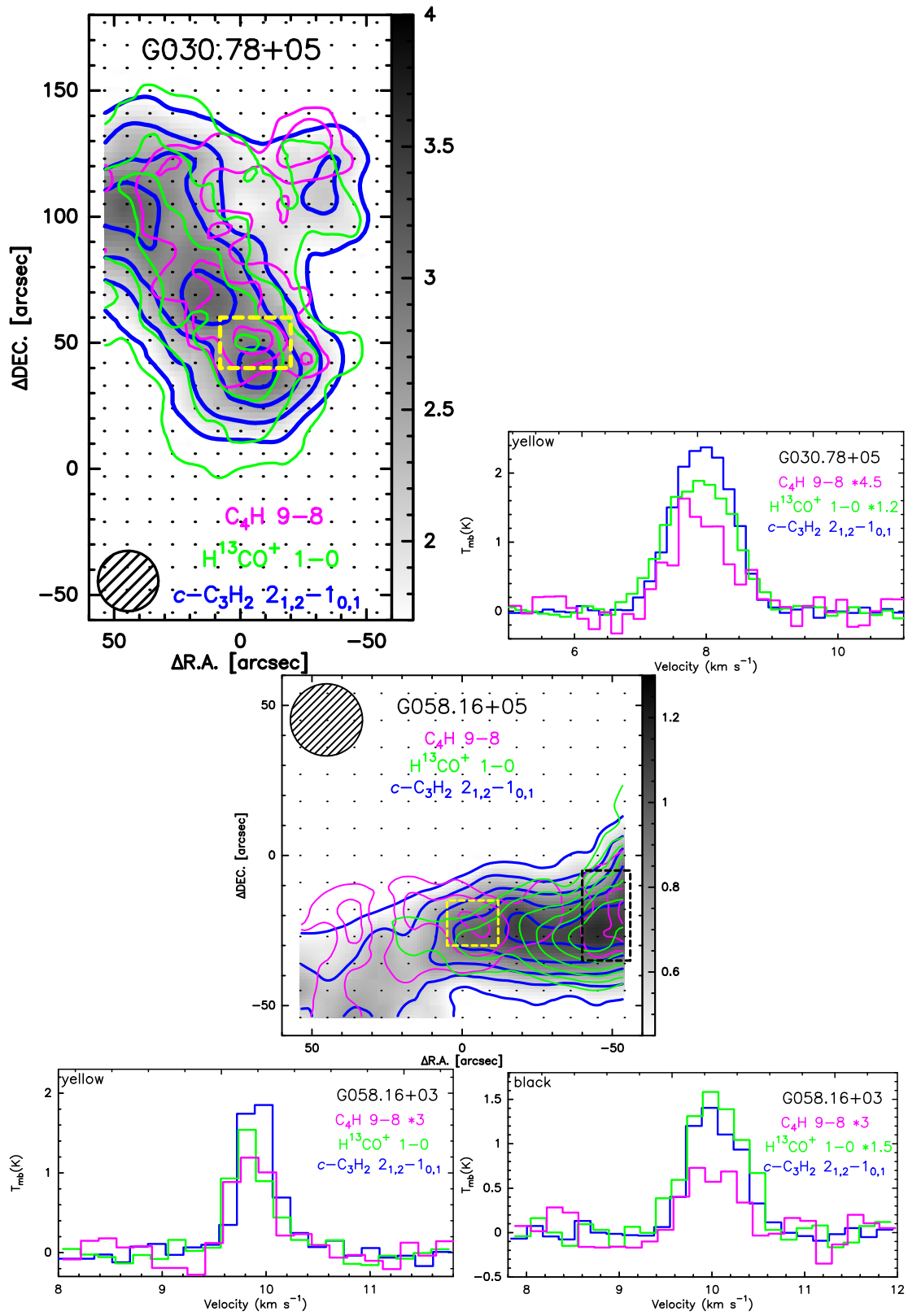


Figure A1. Continued.

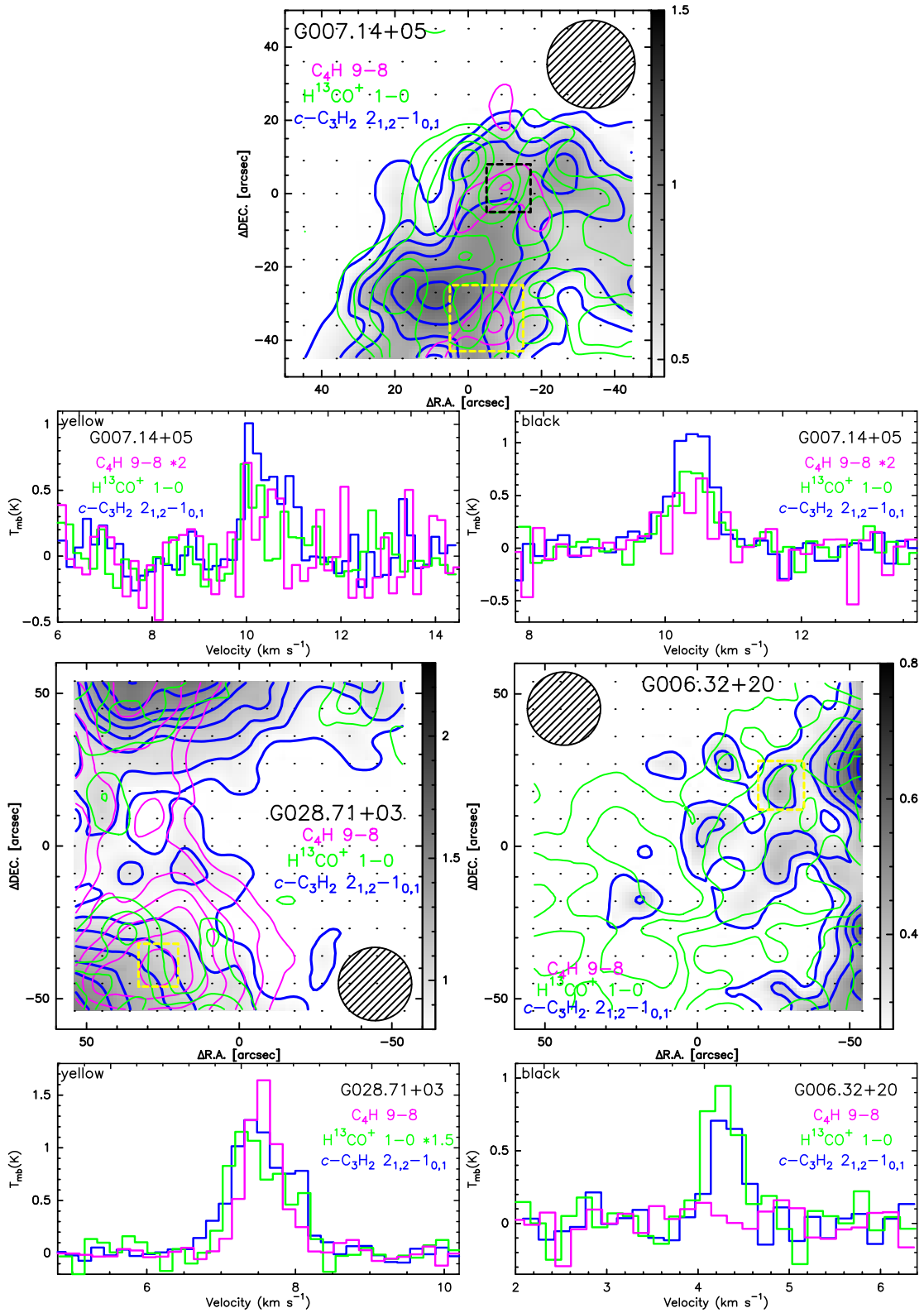


Figure A1. Continued.

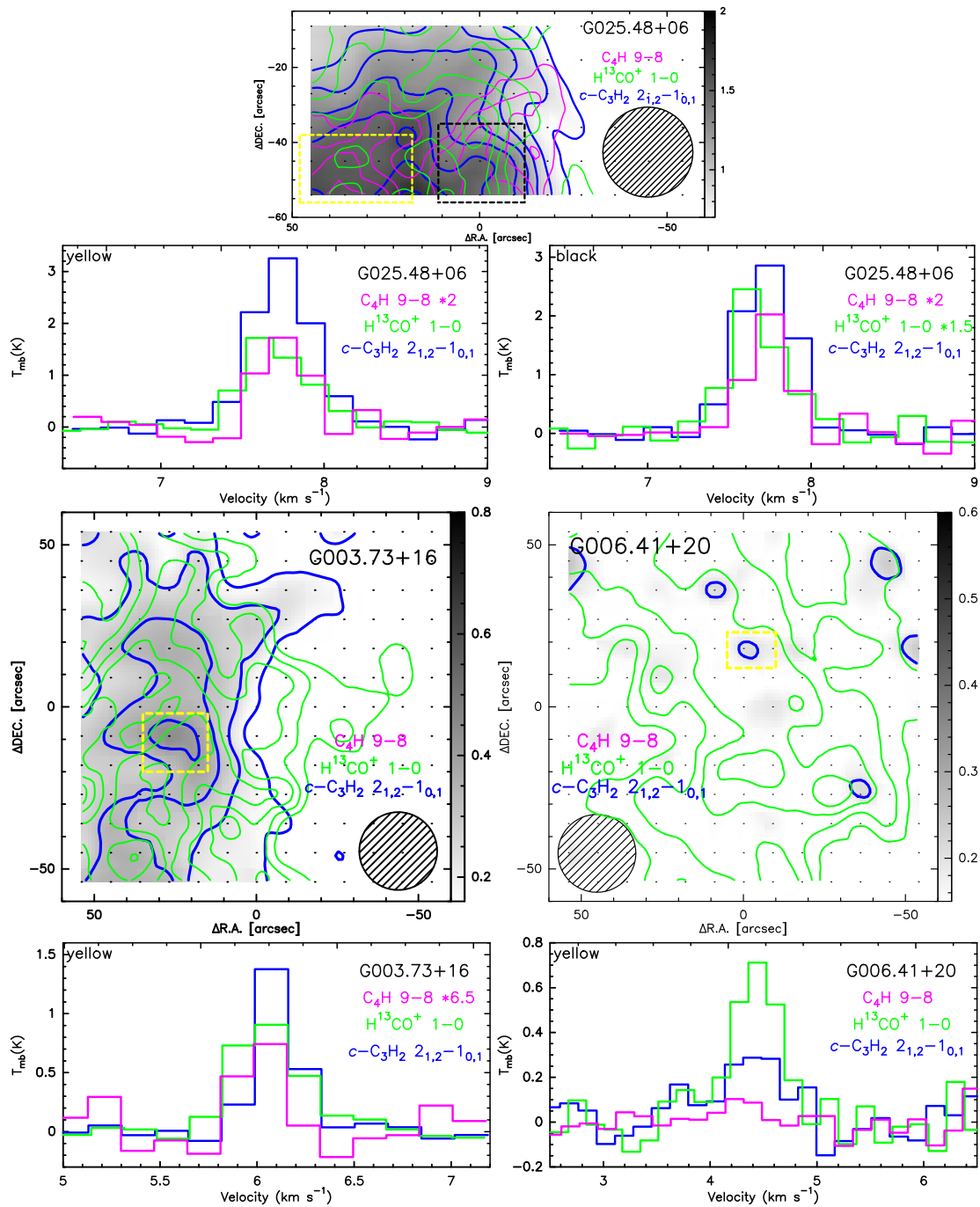


Figure A1. Continued.

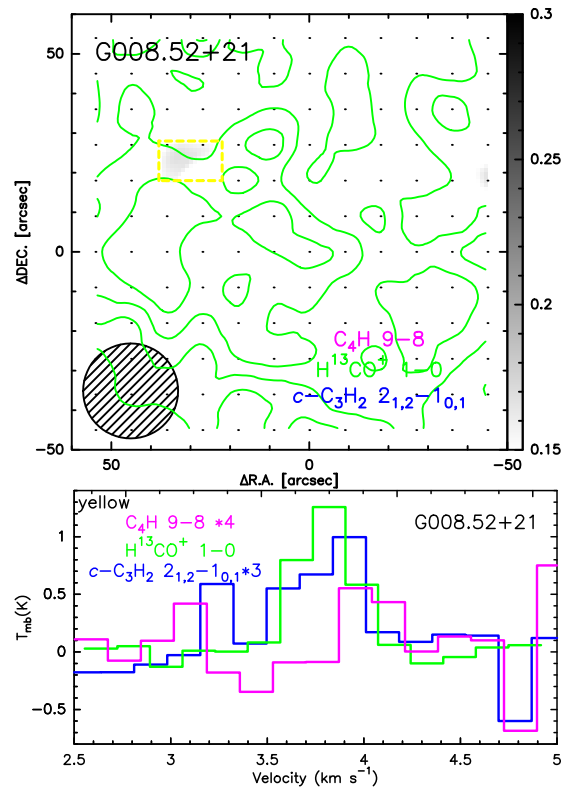


Figure A1. Continued.